Volume 13
Number 15
7 August 2025
Pages 3995-4294

Biomaterials Science

rsc.li/biomaterials-science

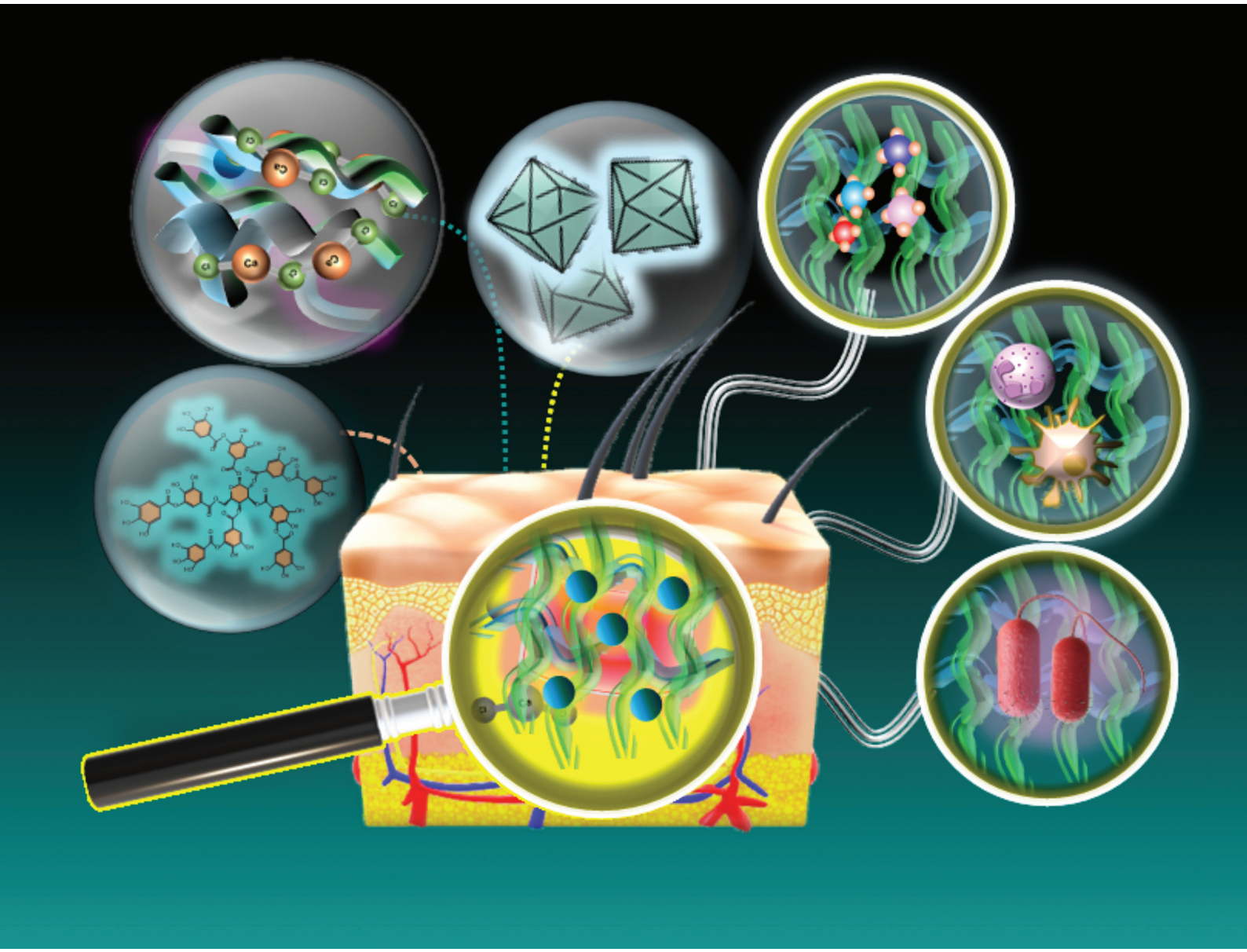

ISSN 2047-4849

PAPER

Yogesh B. Dalvi, Mukesh Dhanka *et al.*
Engineering a bacterial polysaccharide-based metal–organic framework-enhanced bioactive 3D hydrogel for accelerated full-thickness wound healing

ROYAL SOCIETY OF CHEMISTRY

European Society for Biomaterials

Biomaterials Science

ROYAL SOCIETY OF CHEMISTRY

PAPER

View Article Online
View Journal | View Issue

Cite this: *Biomater. Sci.*, 2025, **13**, 4107

Engineering a bacterial polysaccharide-based metal–organic framework-enhanced bioactive 3D hydrogel for accelerated full-thickness wound healing†

Aniruddha Dan,‡[a] Ankita Panigrahi,‡[e] Hemant Singh,‡[a,b,c] Varsha Murali,[e] Manisha Meena,[a] Prateek Goyel,[d] Laxmanan Karthikeyan,[a] Superb K. Misra,[d] Nibu Varghese,[e] Sharlene Sara Babu,[f] Yogesh B. Dalvi *[e] and Mukesh Dhanka *[a]

Hydrogels offer numerous advantages in wound healing, making them a promising alternative to traditional wound dressings. Their biocompatibility and high water content closely resemble natural biological tissues, creating a moist environment that accelerates cell proliferation and tissue repair. Hydrogels maintain optimal hydration levels, preventing wound desiccation and promoting faster healing. Furthermore, their ability to incorporate and deliver therapeutic agents such as antibiotics, anti-inflammatory drugs, or growth factors provides a multifunctional platform for enhanced wound care. Despite these advantages, current clinical wound-dressing materials often fall short in addressing the complexities of wound healing. Hydrogels, with their customizable properties and potential for integration with emerging technologies, represent a significant opportunity to overcome these limitations and improve clinical outcomes in wound management. Herein, we developed a multi-functional Cu-MOF and tannic acid-enriched polymeric hydrogel dressing composed of gellan-gum/zein for full-thickness wound repair. The physical interactions, including electrostatic interaction and hydrogen bonding between the hydrogel components, form a stable hydrogel matrix. The hydrogel exhibits antioxidant properties and antibacterial activity, and is hemocompatible and biocompatible against L929 fibroblast cells. Furthermore, the fabricated hydrogel dressing improvised a full-thickness wound-healing process in rats. Only 1.6% of the wound area was remaining in the case of GG-Z-TA/M1-treated full-thickness wounds in rats. Histopathology images suggest the Cu-MOF-loaded hydrogels aided in extensive re-epithelialization, neovascularization, and hair follicle formation to accelerate the wound-healing process.

Received 25th January 2025,
Accepted 28th April 2025

DOI: 10.1039/d5bm00133a

rsc.li/biomaterials-science

1. Introduction

Wound healing is a highly dynamic and critical process that restores and heals damaged skin and tissues.[1,2] It involves granulation at the wound site through coordinated movement of immune cells, fibroblast cells, collagen, and proteoglycans and the formation of new blood vessels resulting in tissue restoration. Wounds are majorly classified into acute and chronic wounds. The acute wound heals through natural, normal stages of tissue repair, whereas chronic wounds persist for longer periods of time that often lead to physical and emotional distress.[3,4] It is estimated that by 2026, around 20 to 60 million people will have chronic wounds, costing millions of dollars annually.[5] Chronic wounds reduce the regenerative capacity of the skin, which accelerates the growth of opportunistic bacteria, causing the formation of non-healable wounds, and, in many cases, limb amputation is recommended to save

[a]*Department of Biological Sciences and Engineering, Indian Institute of Technology Gandhinagar, Gujarat, India. E-mail: mukesh.d@iitgn.ac.in*
[b]*Department of Biological Sciences, Khalifa University of Science and Technology, Abu Dhabi, United Arab Emirates*
[c]*Center for Biotechnology, Khalifa University of Science and Technology, Abu Dhabi, United Arab Emirates*
[d]*Materials Engineering, Indian Institute of Technology, Gandhinagar-382055, Gujarat, India*
[e]*Pushpagiri Institute of Medical Sciences, Thiruvalla, Pathanamthitta, Kerala, India. E-mail: yogesh_dalvi@pushpagiri.ac.in*
[f]*Department of Oral & Maxillofacial Pathology, Pushpagiri College of Dental Sciences, India*

†Electronic supplementary information (ESI) available. See DOI: https://doi.org/10.1039/d5bm00133a

‡These authors contributed equally.

the life of the patient.[6] Therefore, developing a wound-dressing material that can overcome the limitations of existing conventional dressing methods is very much needed.[7,8]

Hydrogels are considered ideal wound-dressing candidates as they are biocompatible, non-sensitizing, provide moisture for cell proliferation, retain water up to 90%, and have good mechanical strength.[9–12] Gellan gum (GG), an extracellular linear polysaccharide produced by *Sphingomonas elodea* through fermentation, is a water-soluble anionic polymer that interacts with cations or positively charged polymers *via* carboxyl bonds.[13–17] This biopolymer has various applications as it provides several advantages including cell proliferative capability, biocompatibility, antioxidant capacity, and antimicrobial activity.[18–24] Zein (Z) is a hydrophobic natural polypeptide, derived from corn, that is biocompatible and has tissue-engineering applications.[25–29] Moreover, zein has a natural ability to resist microbial attack, is highly stable to thermal changes, and also provides adhesion.[30–32]

Tannic acid (TA), which is found naturally on the bark of trees, is composed of five aromatic rings with dihydroxyphenyl groups and it has numerous benefits.[33–35] TA-based materials have promising applications in biomedical fields as they are stable and nontoxic under *in vitro* physiological conditions. The hydroxyl groups of tannic acid help in coupling with various other materials through the noncovalent interactions of ion coordination and hydrogen bonding.[36–39] Along with these interactions, TA also demonstrates antibacterial activity, free radical scavenging abilities, adhesiveness, which helps in adhesion to the skin, and inhibition of proliferative anaerobic bacteria.[40–44]

Metal–organic frameworks (MOFs) are porous micro/nano structures formed through coordination bonds between inorganic metal ions and organic ligands.[45,46] Numerous materials based on MOFs have been discovered and applied in the fields of chemistry, energy, and biomedicine due to their tunable chemical and physical properties.[47–49] Mainly, the design and structure of MOFs help in the creation of novel functional biomaterials. A variety of MOFs have been developed, namely copper (Cu^{2+}), zinc (Zn^{2+}), silver (Ag^{2+}), that have extensive antibacterial activity as well as antioxidant properties.[50–52] For example, copper is one of the trace elements in the human body and has enormous functionality that helps in cell proliferation and angiogenesis by facilitating release of vascular endothelial growth factors (VEGFs). In addition, copper helps extracellular matrix depositions by stimulating expression of several factors.[53–55] But for its *in vivo* use, the sustained release of copper ions is very much essential. The issues of prolonged copper ion release and organic ligand biocompatibility could be resolved simultaneously by loading MOFs within biocompatible polymeric hydrogels.

This study reports the fabrication of a novel Cu-MOF and TA-loaded bio-polymeric GG and Z hydrogel through physical crosslinking. In this study the Cu-MOF has been encapsulated within a polymeric hydrogel of GG/Z to provide sustained release and enhance the therapeutic efficacy of the copper ions from Cu-MOFs thereby reducing the cytotoxicity caused by excess copper ions. To the best of our knowledge, there have been no reports regarding the fabrication of hydrogels composed of GG/Z. In addition to Cu-MOFs we have added TA as an active compound to further improve the wound-healing potential of the composite hydrogel. Tannic acid also acts as a physical crosslinker to provide the 3D structural network of the hydrogels. The hydrogel displayed efficient antimicrobial activity against both Gram positive and Gram-negative bacteria but was also biocompatible, aided cell migration in fibroblast cell lines and promoted wound healing under *in vivo* conditions through the collaborative action of both copper ions and TA. This study strongly suggests that composite hydrogels possess multifunctional properties and hold great potential as wound dressings for full-thickness wound treatment (Scheme 1).

2. Materials and methods

2.1. Materials

Cupric nitrate trihydrate ($Cu(NO_3)_2{\cdot}3H_2O$), phosphate-buffered saline (PBS), Mueller Hinton agar, Muller Hinton broth, and DMEM were supplied by HiMedia Pvt. Ltd, India. 3-[4,5-Dimethylthiazol-2-yl]-2,5 diphenyl tetrazolium bromide (MTT) and trimesic acid (H_3BTC) were procured from Sigma Aldrich, India. Gelrite gellan gum was supplied by SRL, Pvt. Ltd. Zein protein (M_w: 22–24 kDa) isolated from corn, DPPH (2,2-diphenyl-1-picrylhydrazyl), streptomycin sulphate, and collagenase were procured from Tokyo Chemical Industry. Tannic acid and calcium chloride were provided by LOBA Chemie Pvt. Ltd. Acetic acid (99%), methanol, and ethanol were bought from Finar. Fetal bovine serum (FBS) of US origin was supplied by Gibco. Trypsin was bought from Invitrogen (USA). An L929 mice fibroblast cell line was procured from NCCS, Pune, India. All chemicals were used as received without further purification.

2.2. Synthesis of Cu-BTC MOFs

Cu-MOFs were synthesized according to the protocol mentioned in previous reports.[56,57] Briefly, 25 mL of 5 mM $Cu(NO_3)_2{\cdot}3H_2O$ and 3.5 mM H_3BTC solution was prepared separately in ethanol:distilled water (1 : 1). After both the $Cu(NO_3)_2{\cdot}3H_2O$ and H_3BTC were dissolved properly, they were mixed and stirred for an hour. The solution was then placed in a Teflon container and heated at 100 °C for 18 hours. The product was washed through centrifugation in a mixture of ultrapure water and ethanol (1 : 1) to remove any unreacted precursors or potential guest molecules from the final product. A vacuum oven heated to 60 °C was used to dry the precipitate after centrifugation. The resulting blue powder was activated by being heated at 100 °C in a vacuum for 12 hours. By expelling solvent molecules from the MOF pores, this activation method facilitates the production of

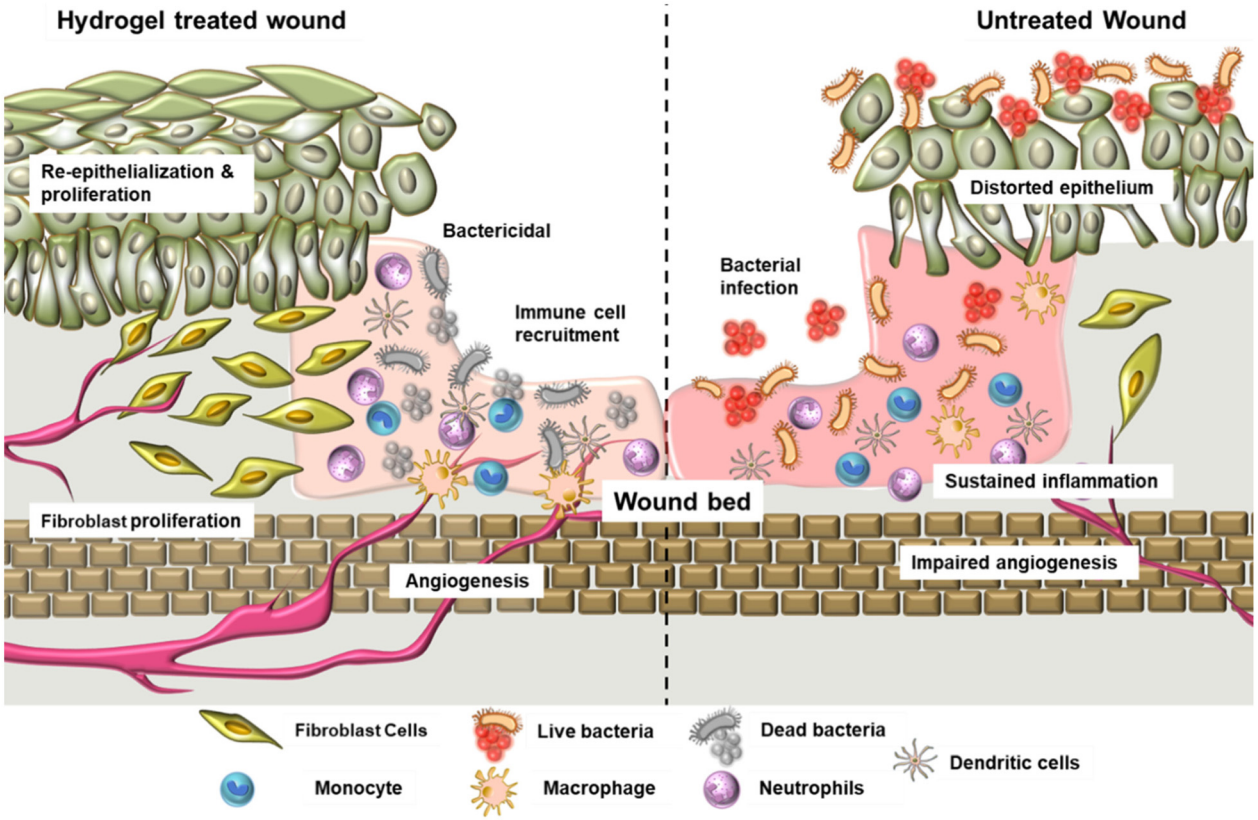

Scheme 1 Schematic illustration of differences between the hydrogel-treated and untreated wound environments.

high-quality crystals with increased porosity and surface area.

2.3. Fabrication of composite polymeric hydrogels

The fabrication of the Cu-MOF and TA-enriched GG/Z-based hydrogel was achieved by physical crosslinking. Briefly, a 1.5% (w/v) aqueous solution of GG was prepared at 70 °C with stirring at 500 rpm, while 2% (w/v) of hydrophobic zein protein was dissolved in a 30 : 70 ethanol and water mixture at room temperature (25 °C). Furthermore, the zein solution was added dropwise into the dissolved GG and stirred well until a homogeneous mixture was achieved. To incorporate TA, 1% (w/v) aqueous solution of tannic acid was added to the prepared mixture. The resulting hydrogel was shaped as desired and allowed to set to form a stable hydrogel at room temperature. To increase the crosslinking further, the prepared hydrogel was immersed overnight in 0.2% $CaCl_2$ solution and then washed thoroughly through rinsing.

To prepare hydrogels containing Cu-MOFs, the same procedure was followed as described above, except that immediately sonicated Cu-MOFs were physically mixed after the addition of tannic acid to the already prepared polymeric solution. Hydrogels containing 0.01%, 0.05%, and 0.1% of Cu-MOFs were named as GG-Z-TA/M1, GG-Z-TA/M2, and GG-Z-TA/M3 respectively.

2.4. Physicochemical characterization of Cu-MOFs

The morphology of the synthesized Cu-MOFs and the fabricated hydrogel was characterized using field emission scanning electron microscopy (JEOL, JSM-7600F, IIT-GN), while elemental analysis was carried out by using an energy dispersive X-ray analysis (EDX) detector. A diluted methanolic solution of Cu-MOFs was drop-cast on glass slides, whereas fabricated hydrogels were lyophilized, and thin cross-sections were chosen for FESEM. Samples of Cu-MOFs and hydrogels were sputter-coated with gold before FESEM imaging. The images were processed through ImageJ software to determine pore sizes. The surface topography of synthesized Cu-MOFs was determined using AFM (Bruker Nano Wizard AFM). FTIR (Fourier transform infrared spectroscopy) analysis of MOFs and the synthesized hydrogel was performed using a Shimadzu FTIR8400s over the wavenumber range of 400–4000 cm^{-1}. UV-visible spectroscopy (JASCO-V-750) analysis was performed to check the ability of the MOFs to absorb or transmit light in the ultraviolet and visible ranges of the electromagnetic spectrum.

The porosity (P) of the fabricated hydrogel ($N = 4$) was determined by the liquid displacement method, as previously explained.[58] In brief, the hydrogels were inserted into a measuring cylinder containing a known amount of ethanol (V_1). After the samples had been positioned inside the cylin-

der, the total volume (V_2) was measured and noted. After the samples were extracted the volume (V_T) was noted. The volume of ethanol remaining in the measuring cylinder is denoted by V_3. The porosity of the hydrogels was calculated through eqn (1):

$$\text{Porosity}\,(\%) = \frac{V_1 - V_3}{V_T} \times 100 \quad (1)$$

In addition, the water retention capacity was determined using the protocol described. To check the water retention capacity of our scaffold, the precise weight of our lyophilized sample was measured before soaking it in PBS (W_{wet}) at room temperature until it fully swelled. Then, after placing tissue paper at the bottom of the centrifuge tube, the hydrogel sample was centrifuged at 500 rpm for 3 min to remove excess water, and the dry weight (W_{dry}) of the sample was measured. Water retention capacity (W_r) was determined through eqn (2):

$$\text{Water retention}\,(\%) = \frac{W_{wet} - W_{dry}}{W_{wet}} \times 100 \quad (2)$$

Furthermore, the swelling behavior of the fabricated hydrogels was assessed as a swelling percentage (S%), which indicates the absorption capacity and hydrophilicity of the samples, as previously conducted.[59] The weight of the lyophilized hydrogel sample (W_d) (N = 5) was measured using an electronic balance before it was dipped in PBS (phosphate-buffered saline at pH 7.4) at room temperature. To obtain W_s, the swollen weight was measured at regular intervals until weight saturation is achieved and no further swelling occurs. The swelling percentage of the hydrogel samples was calculated through eqn (3):

$$\text{Swelling percentage}\,(\%) = \frac{W_s - W_d}{W_d} \times 100 \quad (3)$$

The *in vitro* degradation rate of the fabricated polymeric hydrogels was assessed under both enzymatic and non-enzymatic conditions by calculating the degradation percentage. In brief, the fully swollen hydrogel begins to degrade as increased water content leads to its structural disintegration. The initial weight of the fully swollen hydrogel (W_0) was recorded, and the sample was immersed in PBS of pH 7.4 at 37 °C until its complete degradation, with weight measurements (W_t) taken at regular intervals. For enzymatic degradation, 0.1% (w/v) collagenase was dissolved in PBS, and the same protocol was followed. The degradation rate (%) was measured using eqn (4):

$$\text{Degradation}\ (\%) = \frac{W_0 - W_t}{W_0} \times 100 \quad (4)$$

2.5. Mechanical characterization

The mechanical strength of the fabricated hydrogels was measured using the Universal Testing System (UTS) (Instron 3365 dual column) instrument by performing compression tests. To perform the compression test on the hydrogel formulation, the hydrogel sample (n = 3) of predetermined dimensions (height: 16 mm, width: 12 mm) was placed on a circular plate of 70 mm diameter and compressed by 80% by using another circular plate of 70 mm diameter in parallel above it, at a rate of 5 mm min^{-1}. Furthermore, the compressive stress–strain results obtained were plotted as a curve.

2.6. *In vitro* drug release study

Furthermore, the release behavior of copper ions and TA was determined by calculating the concentration of bioactive agents released, according to previous reports[56] with necessary modifications. A known amount of hydrogel sample (n = 5) was inserted inside a dialysis bag and this was added to PBS solution (10 mL, pH 7.4) and stirred at 37 °C for 6 days. 1 mL of the release media was collected and replaced with an equal volume of fresh PBS after pre-defined time intervals. The collected solution was examined using a UV spectrophotometer (Shimadzu UV 1800) at a wavelength of 280 nm for TA to determine the quantity of TA released from the hydrogel. The concentration of copper ions in the released media was determined through ICP-OES using a Nexion 2000B ICP-MS instrument (PerkinElmer). The cumulative release (%) of TA and Cu ions was determined through eqn (5) using a previously prepared calibration curve:

$$\text{Cumulative release}\ (\%) = \frac{\text{released amount of therapeutic}}{\text{total amount of therapeutics loaded initially}} \times 100 \quad (5)$$

2.7. *In vitro* free radical scavenging activity

The antioxidant properties (free radical scavenging potential) of the gels were assessed by using a 2,2-diphenyl-1-picrylhydrazyl (DPPH) assay analysis. In this assay, each sample (n = 5) was incubated for 90 minutes in the dark in 1 mL of DPPH solution. The optical density values of DPPH solutions were then measured at 517 nm using a UV–vis spectrophotometer (Shimadzu UV 1800). Equal volumes of methanol and DPPH were utilized as the blank and standard, respectively. The DPPH scavenging capacity was computed using eqn (6):

$$\text{DPPH scavenging}\,(\%) = \frac{\text{OD of control} - \text{OD of sample}}{\text{OD of control}} \times 100 \quad (6)$$

2.8. *In vitro* biocompatibility

The percentage hemolysis was used to study the *in vitro* blood-cell compatibility (hemocompatibility assay) of the produced hydrogels as mentioned in the previous literature.[60] Hydrogels were incubated in PBS for 48 hours at 37 °C. Subsequently, goat blood from a local butcher shop was collected into an anticoagulant tube, which was centrifuged for two minutes at 1000 rpm and then washed three times with PBS to extract the red blood cells. The leach-out samples of the respective hydrogels and RBC suspension were then combined in a 1 : 1 volume ratio and stored for 60 minutes at 37 °C. PBS and deionized water were used as the positive and negative controls, respectively. Following centrifugation at 1000 rpm for 5 minutes, the absorbance of the supernatant at 540 nm was

recorded using a UV spectrophotometer. The hemolysis percentage was measured using eqn (7):

$$\text{Hemolysis ratio}\,(\%) = \left(\frac{A_{\text{sample}} - A_{\text{n}}}{A_{\text{p}} - A_{\text{n}}}\right) \times 100\% \qquad (7)$$

A_{s}, A_{p} and A_{n} are the absorbance values of RBCs incubated with hydrogel samples, the positive control and the negative control, respectively.

The cellular viability of the fabricated hydrogel was assessed using the L929 (mice fibroblast) cell line in terms of analysis using the MTT assay. The cells were cultured and maintained in a T25 flask containing Dulbecco's modified Eagle's medium (DMEM) supplemented with 10% fetal bovine serum (FBS) and an antibiotic solution containing penicillin (100 U mL^{-1}), streptomycin (100 μg mL^{-1}), and amphotericin B (2.5 μg mL^{-1}). A one-week-old confluent monolayer of L929 cells was trypsinized, and the cells were suspended in growth medium. A 100 μL cell suspension containing 3×10^4 cells/well was seeded in a 96-well tissue culture plate. The plate was then incubated at 37 °C in a humidified 5% CO_2 incubator. For preparation of the sample, 10 mg of the lyophilized hydrogel was weighed and incubated for 24 hours in 1 mL of DMEM at 37 °C (test by indirect contact). The resulting sample solution was filtered through a 0.22 μm Millipore syringe filter to ensure sterility. The MTT assay was initially performed by adding MTT dye to cells incubated with gels under dark conditions for 4 hours. Then, aliquots were taken out, and a solubilization buffer was pipetted to solubilize the formazan crystals. After that, the absorbance was measured by a microplate reader at 570 nm.[61] Cell viability (%) was determined through eqn (8). Also, a live/dead assay was performed to visualize the morphology of live/dead L929 (mice fibroblast) cells under a fluorescence microscope (OLYMPUS U-HGLGPS) after 24 hours of the different treatments following the procedure as explained in earlier reports.[62,64]

$$\text{Cell viability}\,(\%) = \frac{\text{OD of sample}}{\text{OD of control}} \times 100 \qquad (8)$$

2.9. *In vitro* antibacterial efficacy

The *in vitro* antibacterial activity was determined using the well-diffusion and turbidity methods against both Gram-positive (*Staphylococcus aureus*) and Gram-negative (*Escherichia coli*) strains. For the turbidity measurements, each strain was separately incubated in LB broth, followed by the introduction of the gels. The samples were then incubated at 37 °C in a shaker for 24 hours. Next, a UV–visible spectrophotometer was used to detect the absorbance value of each solution at 625 nm. The formula below (eqn (9)) was used to determine bacterial inhibition:

$$\text{Bacterial inhibition}(\%) = \frac{A_{\text{c}} - A_{\text{s}}}{A_{\text{c}}} \times 100 \qquad (9)$$

Here, A_{c} represents the absorbance values of the untreated bacterial solutions, while A_{s} represents those of the sample-treated bacterial solutions.

In the well-diffusion method, 100 μL of bacterial suspension was cultured on agar plates followed by the creation of wells of 8 mm diameter inside the solidified agar. The hydrogel samples were placed in these wells. The plates were incubated at 37 °C for 16 hours and the bacterial zones were measured using vernier callipers.

2.10. *In vitro* anti-biofilm efficacy

The *in vitro* anti-biofilm potential of the fabricated hydrogel formulations against *E. coli* and *S. aureus* was evaluated through crystal violet (CV) assay. In brief, the hydrogels (2 mL) were incubated with PBS (pH 7.4) for 48 hours to collect the released materials. The leach-out of the hydrogels was incubated with bacterial cells ($\sim1\times10^6$ cfu mL^{-1}) in a 24-well plate for 48 hours at 37 °C under static conditions. Untreated culture media were considered as a negative control. Streptomycin sulphate was considered a positive control. Following incubation, biofilm formation by treated and untreated bacterial cells was assessed using CV staining. The OD of the bacterial culture was recorded at 590 nm using UV-spectrophotometry. Biofilm inhibition (%) was determined through eqn (10),

$$\text{Biofilm mass}\ (\%) = \frac{(\text{OD}_{\text{s}} - \text{OD}_{\text{n}})}{\text{OD}_{\text{n}}} \times 100 \qquad (10)$$

where OD_{s} and OD_{n} are the absorbance values of the hydrogel-treated bacterial culture and the untreated bacterial culture, respectively.

2.11. *In vivo* wound-healing study

Four rats (Sprague–Dawley) used in this study were obtained from the Pushpagiri Institute of Medical Sciences and Research Centre, Tiruvalla, Kerala, India. The age of the rats was 8–10 weeks, with a weight range of approximately 200–300 g. Until the completion of the experiment, the animals were housed in distinct cages. Before conducting experiments, ethical approval was obtained from the IAEC (Institutional Animal Ethics Committee) of the PIMC&RC (602/PO/Re/S/02/CPCSEA). All methods used in this study strictly followed the National Institutes of Health Guidelines for the care and use of laboratory animals. The animals were acclimatized to their environment for 2 weeks, and then the wound-healing study was performed. Intraperitoneal anesthesia (ketamine hydrochloride 50 mg kg^{-1} and xylazine 5 mg kg^{-1}) was administered before surgical procedures were started. The dorsal surface of the animal was shaved using a sterile blade and povidone-iodine was used to disinfect the dorsal area. Biopsy punches (10 mm) were used to create full-thickness wounds on the shaved dorsal skin of each rat, as mentioned in earlier literature.[62] The wound of one of the four animals was treated with GG-Z-TA-M3 (Test), with GG-Z-TA (Blank) administered to the second, with a third animal as positive control after treatment with commercially available Silverex and the fourth rat as negative control (treated with normal saline). The wound of each rat was then covered with surgical tape (Tegaderm). Macroscopic images of the wounds were captured

on day 0, day 5, day 10, day 15, and day 20 to monitor the wound-healing progress. Wound contraction was determined by processing the wound images through ImageJ software. The wound contraction (%) was determined through eqn (11):

$$\text{Wound contraction}\,(\%) = \left(\frac{\text{initial wound area on day 0} - \text{wound area on day } n}{\text{initial wound area on day 0}}\right) \times 100 \quad (11)$$

The animals were sacrificed on the 21st day and tissue samples were collected from the wound area. Histopathological analysis was performed using hematoxylin and eosin. Images were captured with an Olympus light microscope, and these were further analyzed for different parameters including re-epithelialization, infiltration of inflammatory cells, blood vessel formation *etc*.

2.12. Statistical analysis

For a small number of data groups (n = 3), non-parametric (Kruskal–Wallis) statistical analysis was used in Origin 9 and Microsoft Excel was used to provide quantitative findings. However, a large number (n = 10) of data groups were subjected to analysis of variance (ANOVA) and a t-test. The findings were reported as means and standard deviations (SD). A significant difference was defined as one with a probability (p) value of <0.05.

3. Results and discussion

3.1. Physicochemical characterization of the synthesized Cu-MOF

Cu-centred MOFs were synthesized by achieving co-ordination between Cu ions and carboxylate groups present in the BTC during a hydrothermal reaction, as presented in Fig. S1.† The FT-IR spectrum (Fig. S2†) of the Cu-MOF exhibits a broad peak between 3400 cm^{-1} and 2640 cm^{-1} due to O–H stretching. The prominent peaks observed at 1444 cm^{-1} and 1647 cm^{-1} are due to the asymmetric stretching of the carboxylate groups of benzene tricarboxylate ligands. The distinctive peaks at 1369 cm^{-1} are produced due to the symmetric stretching of the carboxylate group (–COOH).[63] The peaks at 489 cm^{-1} and 729 cm^{-1} are observed due to the Cu–O vibration.[64,65] Fig. S3† shows the XRD spectra of the Cu-MOF. The diffraction peaks observed at 6.6°, 9.4°, 11.5°, 13.38°, 14.5°, and 18.9° correspond to the crystalline planes (200), (220), (222), (400), (331) and (440) of the face-centred cubic crystal structure of synthesized Cu-MOFs, in accordance with the previous literature.[57,65]

The TGA plot (Fig. S4†) reveals minor weight loss (~20%) below 200 °C, mainly because of the evaporation of the solvent molecules, followed by major weight loss between 250 °C to 500 °C due to degradation of the framework, confirming the formation of thermostable Cu-BTC MOFs through coordination between Cu ions and organic ligands (BTC). UV spectra (Fig. S5†) of synthesized Cu-MOFs exhibit a distinct peak at 477 nm. The synthesized Cu-MOF was investigated for shape, size, morphological features, and elemental composition through FESEM, bio-AFM, and EDS. The FESEM image shown in Fig. S6† and the AFM image (Fig. S7†) exhibit the octahedral structure of the synthesized Cu-MOF, where the edge of the octahedral structure is 5–15 μm, which is consistent with values in the reported literature.[66–68] The magnified image shown in Fig. S9† reveals that the octahedral Cu-MOF has a porous, broad surface area, which will further enhance the bactericidal effect.[69] The EDX spectra shown in Fig. S8† depict the atomic percentages of the elements present in the Cu-MOF, *i.e.* carbon (70.8%), oxygen (20.6%), and copper (8.6%), confirming the successful synthesis of the Cu-MOF. Fig. S10† also shows the presence of different elements, such as carbon, oxygen, and copper in the Cu-MOF.

3.2. Fabrication and physicochemical characterization of hydrogels

Cu-MOFs, TA-integrated GG and Z-based physically crosslinked hydrogels were successfully fabricated with different concentrations of MOFs, as depicted in Fig. 1A. The composite hydrogel was fabricated successfully by physically crosslinking GG and Z, and incorporating the bioactive compounds TA and Cu-MOF. Crosslinking was performed using calcium to increase the mechanical strength further. Four hydrogel samples were prepared with varying concentrations of Cu-MOFs, *i.e.*, 0.01% (w/v), 0.05% (w/v), and 0.1% (w/v) %, named as GG-Z-TA/M1, GG-Z-TA/M2, and GG-Z-TA/M3, respectively, and one hydrogel without the copper MOF, *i.e.*, GG-Z-TA. Fig. S11† shows the FTIR spectra of GG, zein, TA, and the fabricated hydrogels. The FTIR spectrum of GG shows characteristic bands at 3348 cm^{-1} and 2926 cm^{-1}, attributed to the vibration of –OH and $-CH_2$ groups. Also present are bands at 1610 cm^{-1} and 1413 cm^{-1} attributed to symmetric and asymmetric –C═O stretching of the carboxylate anion groups[70]. The FTIR spectrum of zein reveals a band at 3299 cm^{-1} for the amide bond (N–H stretching vibration). The band at 2960 cm^{-1} is attributed to C–H stretching vibration. The band present at 1652 cm^{-1} indicates the stretching vibration of amide I and C═O. Also, the band present at 1539 cm^{-1} is attributed to amide II and the C–N bond stretching vibration.[71] The FTIR spectrum of TA exhibited characteristic bands of typical polyphenols, including a broad band from 3000–3500 cm^{-1} attributed to –OH stretching, and a peak at 1709 cm^{-1} assigned to the stretching vibration of –C═O groups. The characteristic bands observed at 1607 cm^{-1},1529 cm^{-1} and 1448 cm^{-1} are ascribed to benzyl stretching while the band at 758 cm^{-1} is due to the scissoring vibration of trisubstituted benzene rings.[72] The GG-Z-TA FTIR spectrum shows the presence of bands that are characteristic of GG, zein and tannic acid with minor shifts indicating the H-bonding between all three compounds. Comparing the spectra of GG-Z-TA with Cu-MOF-loaded cryogels, the prominent difference is the presence of characteristic bands at 1654 cm^{-1} and 1371 cm^{-1}, which is due to the stretching vibration of the $-COO^-$ of the organic

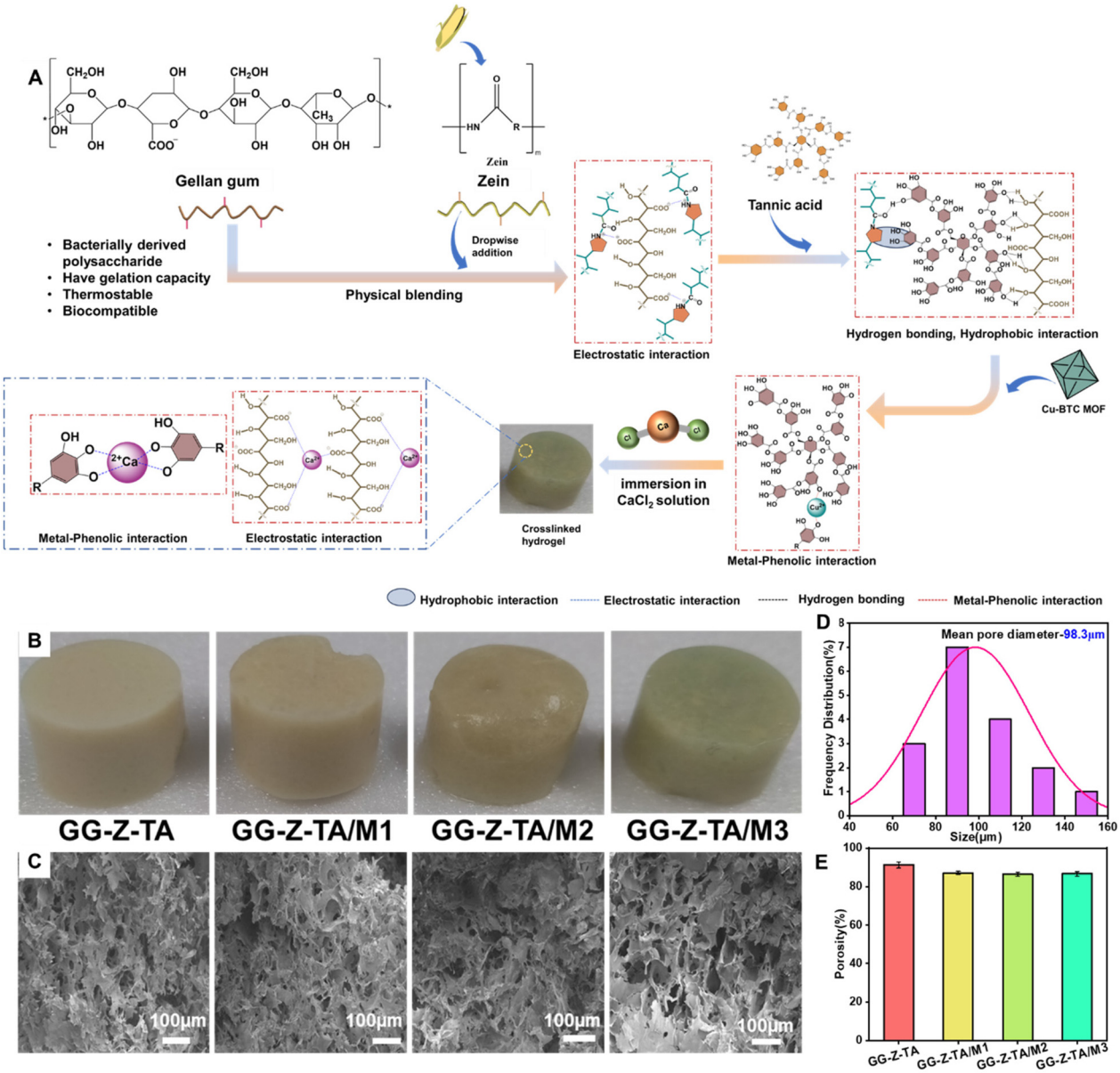

Fig. 1 (A) Scheme showing the fabrication of Cu-BTC MOF-loaded hydrogels. (B) Macrograph of fabricated hydrogels. (C) FESEM images of fabricated hydrogels. (D) Pore diameter of fabricated hydrogels. (E) Porosity (%) of fabricated hydrogels. Columns/lines and bars represent the mean and standard deviation, respectively, whereas ***$p < 0.0005$ signifies the statistical difference.

ligand (BTC) confirming the physical loading of the Cu-MOFs within the hydrogel.

The physical appearances of the hydrogels can be seen in Fig. 1B. To reveal the internal morphology, the cross-section of each hydrogel was analyzed using FESEM, as shown in Fig. 1C. The internal microstructure reveals that the hydrogel is porous in nature with interconnected micropores. These interconnected pores will aid the hydrogel in accelerating wound healing as these will help in retaining water, providing a moist environment that will promote re-epithelialization. Moreover, pores will provide a scaffold for migration and proliferation of fibroblasts and keratinocytes,[73,74] cell growth, and nutrient and gaseous exchange. For cellular functions, morphological features and porosity are very much essential not only to mimic the morphology of the ECM but also to provide suitable porosities and pore sizes for efficient cell infiltration and enhanced transport of nutrients.

The FESEM images were analyzed using ImageJ software; Fig. 1D reveals that the mean diameter of the pores present in the hydrogel is 98.3 μm. There are several literature sources stating that hydrogels having pore sizes in the range of 30 μm–200 μm support proliferation,[75] and migration of dermal fibroblast cells,[76] while also promoting vasculature formation[77] and re-epithelialization[78] ultimately leading to accelerated wound

healing.[79,80] So, the pore size of the fabricated hydrogel is suitable for efficient wound healing. The porosity (%) of the fabricated hydrogel was analyzed using the liquid displacement method; the porosity (%) for the fabricated hydrogel formulations are 91.3%, 87%, 86.3%, and 85.7% for GG-Z-TA, GG-Z-TA/M1, GG-Z-TA/M2, and GG-Z-TA/M3, respectively (Fig. 1E). The porosity (%) of GG-Z-TA is slightly higher than that of hydrogels containing Cu-MOFs; however, there is no significant decrease in the porosity percentage when the concentration of Cu-MOFs is increased. However, the porosity values (%) of the hydrogels are sufficient to assist in the wound-healing process. The water retention capacity can be seen in Fig. 2A. The decreasing order of the water retention capacity is GG-Z-TA (557.5%) > GG-Z-TA/M1 (470.1%) > GG-Z-TA/M2 (400.9%) > GG-Z-TA/M3 (305.4%). The water retention capacity of the fabricated hydrogels decreases gradually with increasing concentration of Cu-MOFs. Furthermore, to depict the hydrophilic nature of the fabricated hydrogels, their swelling (%) was determined. From the Fig. 2B, it can be interpreted that hydrogels are hydrophilic in nature. The hydrophilic nature of the hydrogel is beneficial in wound healing as it maintains a moist environment that accelerates wound healing and further helps with nutrient supply.[74] The swelling (%) decreases gradually as the concentration of Cu-MOFs increases, which might be due to the addition of hydrophobic groups since trimesic acid has an aromatic ring that can decrease the swelling percentage; loss of swelling can also be associated with the rigidity of the aromatic ring, and due to that, the water retention capacity of the hydrogel also decreases. Analysis of the biodegradability of the fabricated polymeric hydrogel, *via* non-enzymatic degradation (Fig. 2C) and enzymatic degradation with 0.1% collagenase (Fig. 2D), was conducted. Fig. 2C shows that GG-Z-TA was completely degraded in 16 days, whereas GG-Z-TA/M1, GG-Z-TA/M2, and GG-Z-TA/M3 were degraded in 13 days, 12 days and 11 days, respectively, under non-enzymatic conditions. However, in the presence of collagenase, the degradation of the polymeric hydrogels was accelerated as depicted in Fig. 2D, which might be due to the protease activity of the collagenase on the protein component of the (Z)-fabricated hydrogels. Under both conditions, the degradation tendency of the hydrogels increased with increasing concentration of Cu-MOFs, with the degradation rate increasing gradually. This may be due to the release of copper ions and TA, which disrupts the physical interactions that keep the hydrogel stable, causing the hydrogels to lose their 3D structural integrity.

3.3. Mechanical characterization

The fabricated polymeric hydrogel-based wound dressings should have desirable mechanical properties to withstand the pressure created by frequent body movement, so that the hydrogels can maintain their structural integrity and continue their healing of the wound. To investigate the mechanical features of the fabricated hydrogel formulations, compressive stress–strain tests on these hydrogels were performed. Fig. 2E shows the compressive strain–stress plot of these hydrogels. All fabricated nano-composite hydrogels reveal typical "J"-shaped curves, confirming their tolerance toward compressive stress. GG-Z-TA exhibited compressive stress of 0.654 MPa at 88% strain. GG-Z-TA/M1, GG-Z-TA/M2, and GG-Z-TA/M3 exhibited compressive stress of 0.985 MPa, 1.24 MPa, and 3.943 MPa, respectively. The compressive stress tolerance capacity of the hydrogels increased with an increase in concentrations of Cu-MOFs. GG-Z-TA/M3 exhibited excellent compressive stress of 3.943 MPa, which is almost seven times that of the compressive stress of GG-Z-TA. This increase in compressive stress tolerance might be due to increases in interaction due to there being more metal–phenolic co-ordination between Cu ions and TA together with the increase in concentration of Cu-MOFs.

3.4. *In vitro* release study

The cumulative release of TA and Cu ions can be seen in Fig. 2F and G, respectively. Both TA and Cu ions were released from the hydrogel in a sustained manner for more than 96 hours. The increasing order of cumulative release of TA follows GG-Z-TA (52.46%) < GG-Z-TA/M1 (88.67%) < GG-Z-TA/M2 (93.91%) < GG-Z-TA/M3 (98.65%) as shown in Fig. 2F. This release behavior can be attributed to the pH (7.4) of the release media, whereupon the phenolic –OH groups in the TA structure are converted into quinone, leading to reduction of the interaction of TA with other components of these hydrogels, ultimately resulting in increased release of TA from the hydrogels. The increasing order of cumulative release of Cu ions follows GG-Z-TA/M1 (85.29%) < GG-Z-TA/M2 (89.64%) < GG-Z-TA/M3 (93.18%), as shown in Fig. 2G. It can be interpreted from Fig. 2G that as the concentration of the copper MOF increases, the cumulative release (%) also increases gradually. This might be due to the degradation of the benzene-1,3,5-tricarboxylate (BTC), leading to disruption of the Cu-MOFs, which ultimately results in the release of Cu ions from the hydrogels.

3.5. *In vitro* antioxidant activity

In cases of chronic wounds, one of the main causes of deteriorating wound conditions is unrestrained production of free radicals. So, to accelerate the wound-healing mechanism, the biomaterials should have antioxidant properties. In this study, DPPH was used as a free radical, and the free radical scavenging capacity of the hydrogels was determined through the DPPH scavenging capacity. Fig. 2H and I show the DPPH scavenging capacity of the fabricated polymeric hydrogels. In Fig. 2I, it is shown that with increasing incubation time period, the remaining DPPH concentration (%) has been diminished. After 30 minutes of incubation, the remaining DPPH concentrations (%)in the GG-Z-TA, GG-Z-TA/M1, GG-Z-TA/M2, and GG-Z-TA/M3 hydrogel-treated DPPH solutions were 28.06%, 25.09%, 20.05%, and 16.75%, respectively. After 3 hours of incubation, the remaining DPPH concentration (%) further dwindled to 7.92%, 5.73%, 4.89%, and 2.94% for the GG-Z-TA, GG-Z-TA/M1, GG-Z-TA/M2, GG-Z-TA/M3 hydrogel-treated DPPH solutions, respectively. The DPPH scavenging activity is mainly due to the presence of well-known plant-

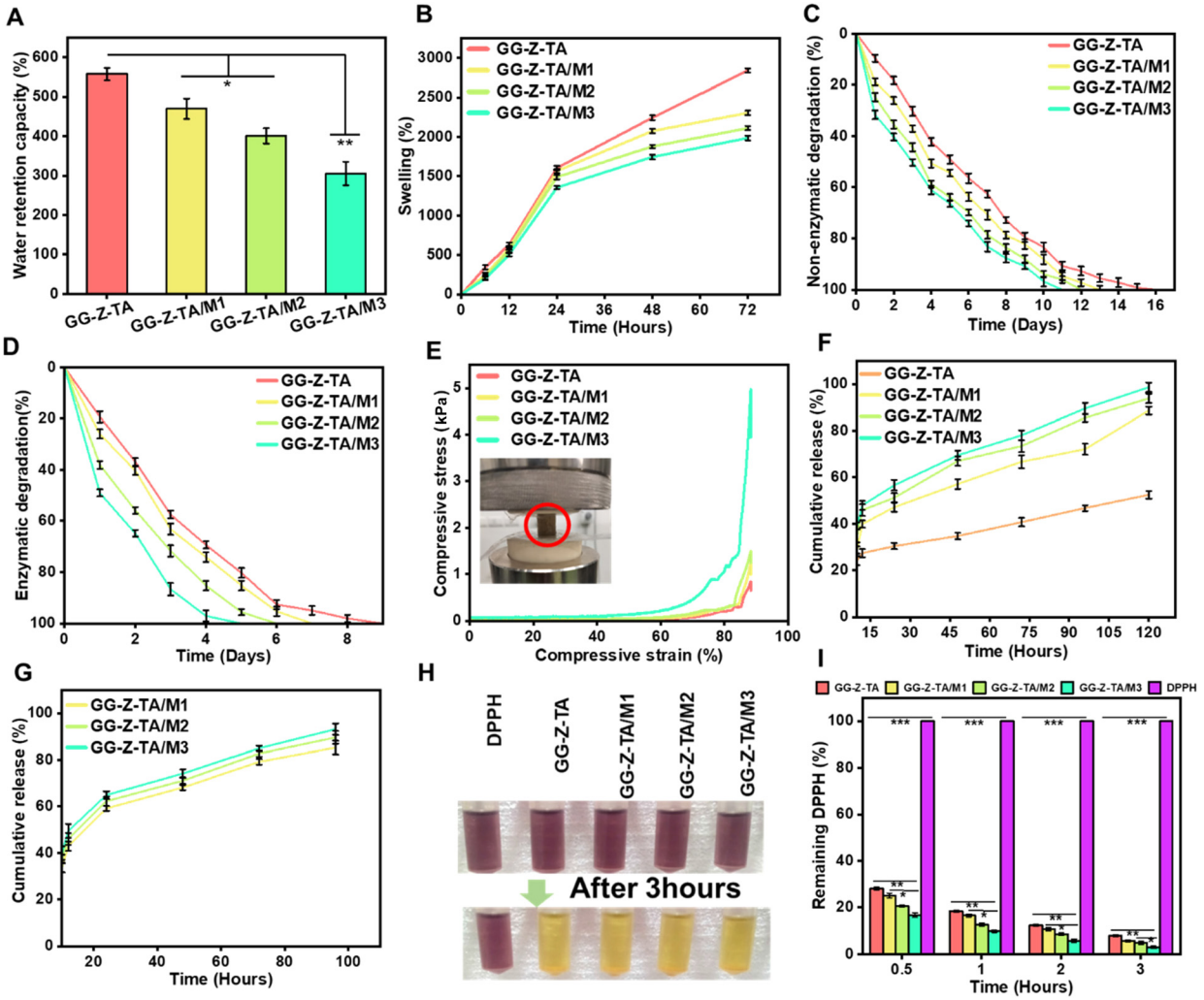

Fig. 2 (A) Water retention capacity (%) of the hydrogels. (B) Swelling (%) capacity of the hydrogels. (C) Non-enzymatic degradation (%) of fabricated hydrogels. (D) Enzymatic degradation (%) of composite hydrogels. (E) Compressive strain–stress curve of fabricated hydrogels. (F) Cumulative release (%) of tannic acid from polymeric hydrogels. (G) Cumulative release (%) of copper ions from polymeric hydrogels. (H) Images of DPPH scavenging activity by fabricated polymeric hydrogels (after 3 hours of incubation). (I) DPPH scavenging (%) by polymeric hydrogels.

derived polyphenolic TA molecules,[81] and the variation in the DPPH scavenging ability is due to the difference in the released amount of tannic acid from the fabricated hydrogels. Also, due to the scavenging of DPPH, the color of the hydrogel-treated DPPH solutions changed from deep purple to yellow, whereas the untreated DPPH solution remains deep purple, as shown in Fig. 2H.

3.6. *In vitro* biocompatibility

To be selected as ideal wound dressings, biomaterials should be biocompatible. So, to investigate the biocompatibility of the hydrogels, hemolysis and MTT assays were performed. First, any deleterious effects of the fabricated hydrogels on red blood cells (RBCs) were determined. Fig. 3A and B show the hemocompatibility of the fabricated hydrogels. In the macrographic picture of Fig. 3A, distinct pellets of RBCs can be observed in PBS, GG-Z-TA, GG-Z-TA/M1, GG-Z-TA/M2, and GG-Z-TA/M3-treated RBCs, in contrast to de-ionized water-treated RBCs where the bright red supernatant can be observed due to extensive hemolysis. The results of the quantitative analysis of hemolysis are shown in Fig. 3B. Hemolysis (%) caused by GG-Z-TA, GG-Z-TA/M1, GG-Z-TA/M2, and GG-Z-TA/M3 is 1.27%, 2.35%, 2.8%, and 4.5% respectively. It can be observed that with increasing concentration of loaded Cu-MOFs, the extent of hemolysis (%) has been increased, which might be due to the interaction between (positively) charged Cu^{+} ions and the (negatively) charged RBC membrane. However, as per ASTM standard F756, all the hydrogel formulations are hemocompatible as all of four hydrogels have caused hemolysis of <5%.

Furthermore, an MTT assay was performed to investigate the cytotoxicity of the fabricated hydrogels against L929 fibroblast cells. Fig. 3C shows the quantitative analysis of cell viability (%). It depicts that with increasing incubation time, hydro-

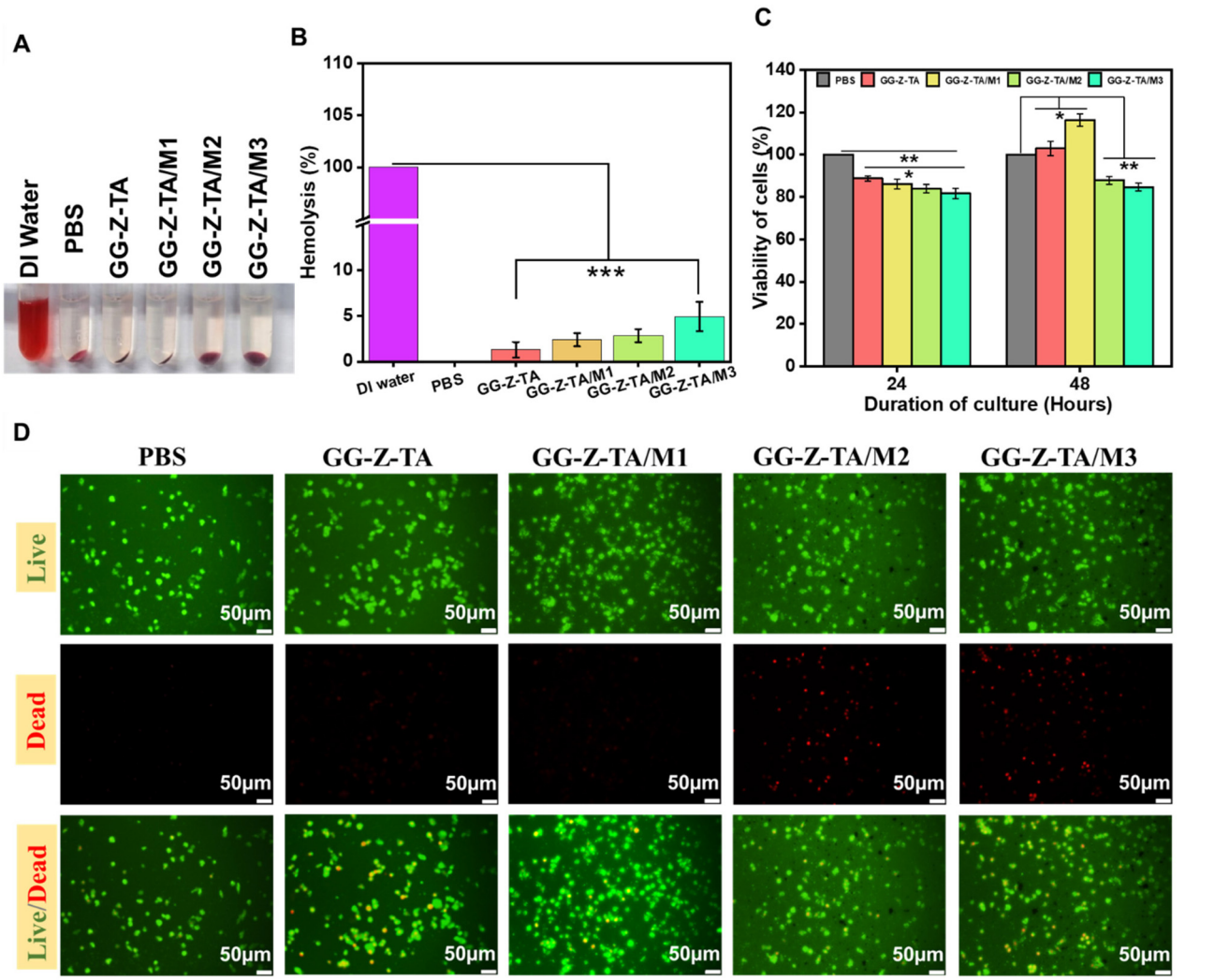

Fig. 3 (A) Macrographic images of hemolysis caused by the fabricated nano-composite polymeric hydrogels. (B) Quantitative analysis of hemolysis by different formulations of fabricated nano-composite polymeric hydrogels. (C) Quantitative analysis of MTT assay against L929 cells treated with fabricated nano-composite polymeric hydrogels. (D) Live/dead cell assay with fabricated hydrogel systems. Here, columns and error bars represent the mean and standard deviation, whereas $*p < 0.05$, $**p < 0.005$, and $***p < 0.0005$ show the statistical difference.

gels support greater cell growth. After 48 hours, GG-M-TA/M1 exhibited the highest growth in the number of L929 cells in terms of mitochondrial activity as detected *via* the MTT assay compared to the other hydrogel formulations. It can be observed that in hydrogels with a lower concentration of Cu-MOFs, the hydrogel has a supportive effect on cell growth. Also, the morphology of seeded L929 cells on the different hydrogel formulations was evaluated using a live/dead staining assay, as shown in Fig. 3D. Histological staining provides diverse insights into interactions between L929 cells and hydrogel formulations, such as cellular distribution, morphology, and cell spreading. The images of stained live cells reveal that no significant morphological defects are observed in the cells treated with all hydrogel systems. However, slight toxicity was observed as the number of dead cells increased with increasing concentrations of Cu-MOFs within the hydrogel formulations, as was similarly observed in the MTT assay. Hydrogels containing higher concentrations of the Cu-MOFs (GG-Z-TA/M2, GG-Z-TA/M3) exhibit reduced cell growth, indicating toxicity towards L929 cells as well as RBCs. Therefore, the formulation GG-Z-TA/M1 was selected as the most bio-compatible for the *in vivo* studies.

3.7. *In vitro* antibacterial activity

Due to the formation of wounds, the skin loses its structural and functional integrity and becomes susceptible to bacterial infection. So, the antibacterial efficacy of the fabricated hydrogels against both Gram-positive (*S. aureus*) and Gram-negative (*E. coli*) bacteria was investigated. Fig. 4A–C demonstrates the antibacterial efficacy of fabricated hydrogels against *E. coli*. Fig. 4A represents the quantitative analysis of bacterial inhibition (%) of *E. coli* by fabricated hydrogels. GG-Z-TA, GG-Z-TA/M1, GG-Z-TA/M2, and GG-Z-TA/M3 were able to kill 70.33%, 84.67%, 92.5%, and 98.9% of the *E. coli* bacterial population,

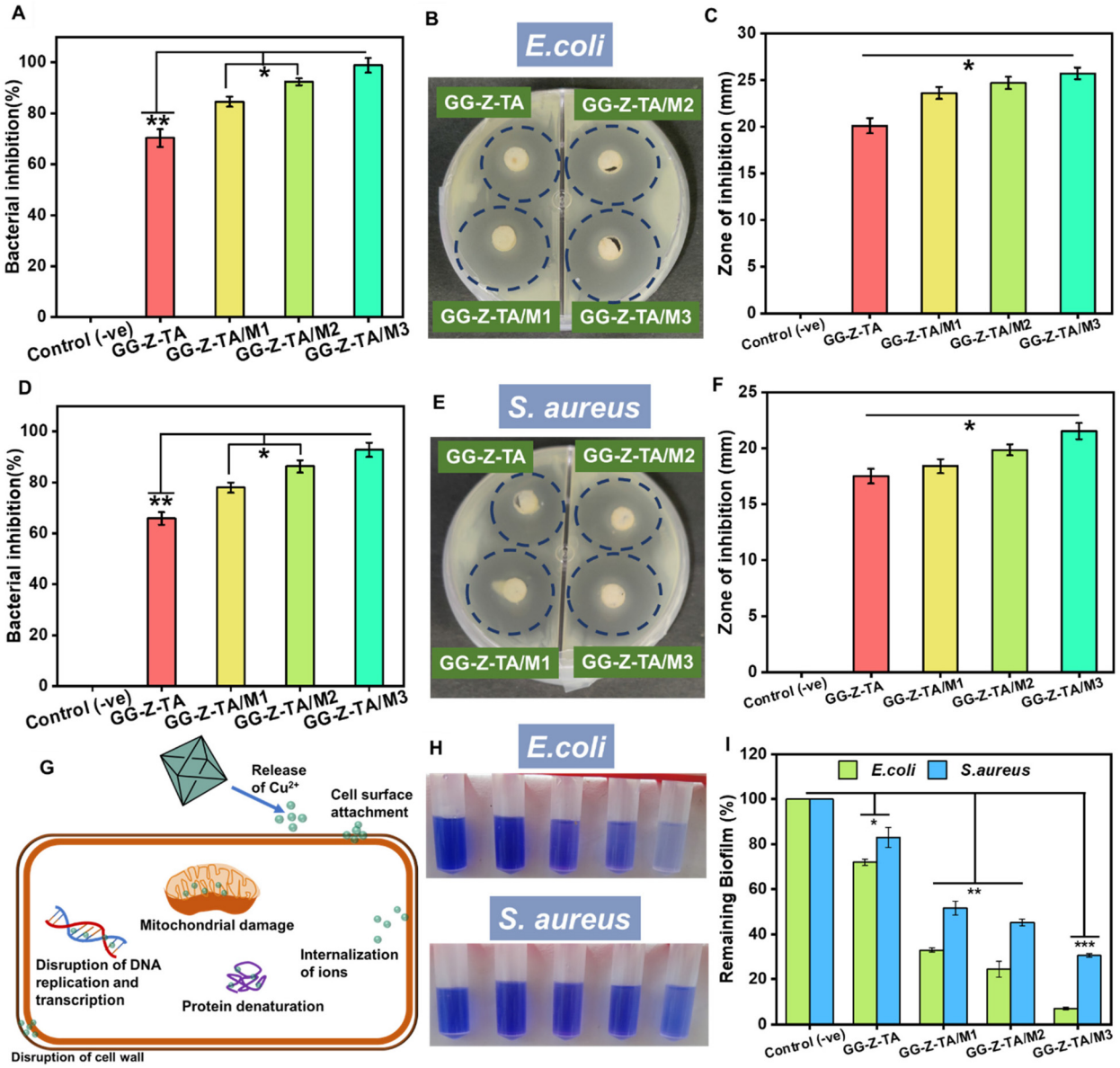

Fig. 4 (A) Quantitative analysis of bacterial inhibition (%) by fabricated nano-composite polymeric hydrogels against *E. coli*. (B) Image showing zones of inhibition formed by nano-composite polymeric hydrogels against *E. coli*. (C) Quantitative analysis of zones of inhibition created by by nano-composite polymeric hydrogels against *E. coli*. (D) Quantitative analysis of bacterial inhibition (%) by fabricated nano-composite polymeric hydrogels against. *S. aureus*. (E) Image showing zones of inhibition formed by nano-composite polymeric hydrogels against *S. aureus*. (F) Quantitative analysis of zones of inhibition created by by nano-composite polymeric hydrogels against *S. aureus*. (G) Mechanism of anti-bacterial activity of Cu ions. (H) Macrographic image of anti-biofilm activity of nano-composite polymeric hydrogels. (I) Quantitative analysis of anti-biofilm activity of nano-composite polymeric hydrogels. Here, columns and error bars signify the mean and standard deviation, whereas $*p < 0.05$, $**p < 0.005$, and $***p < 0.0005$ show the statistical difference.

respectively. Fig. 4B shows distinct zones of inhibition created by the fabricated hydrogels against *E. coli*. Fig. 4C shows the level of GG-Z-TA, GG-Z-TA/M1, GG-Z-TA/M2, and GG-Z-TA/M3-created zones of inhibition with respective diameters of 20.12 mm, 23.64 mm, 24.71 mm, and 25.73 mm against *E. coli*. Fig. 4D–F demonstrates the antibacterial efficacy of fabricated hydrogels against *S. aureus*. As shown in Fig. 4D, GG-Z-TA, GG-Z-TA/M1, GG-Z-TA/M2, and GG-Z-TA/M3 were able to kill 65.89%, 78.01%, 86.33%, and 92.9% of the *S. aureus* bacterial population, respectively. Fig. 4E shows distinct zones of inhibition created by fabricated hydrogels against *S. aureus*. Fig. 4F shows the level of GG-Z-TA, GG-Z-TA/M1, GG-Z-TA/M2, and GG-Z-TA/M3-created zones of inhibition with respective diameters of 17.52 mm, 18.4 mm, 19.84 mm, and 21.52 mm against *S. aureus*. From both the well-diffusion study and turbidity method, it is obvious that fabricated Cu-MOF-loaded

polymeric hydrogels exhibit efficient antibacterial activity against both *E. coli* and *S. aureus*. The antibacterial effect of the nano-composite polymeric hydrogel was due to the synergistic antibacterial activity of zein protein, polyphenolic TA, and Cu-MOFs. Antibacterial activity of Z against *E. coli* has been mentioned in previous literature. TA has antibacterial effects against both Gram-positive and Gram-negative bacteria.[82] Cu-MOFs have been used as sources of Cu ions where Cu ions exert antibacterial activity through DNA structure degradation, which alters the permeability of bacterial cell walls leading to bacterial cell lysis, as shown in Fig. 4G.[83–85]

3.8. *In vitro* anti-biofilm efficacy

Through the crystal violet staining technique, the anti-biofilm efficacy of the fabricated hydrogel formulations was evaluated. Mature *E. coli* and *S. aureus* biofilms were grown and incubated with different hydrogel formulations. As Fig. 4I reveals, the untreated group (control (–ve)) has 100% of the biofilm

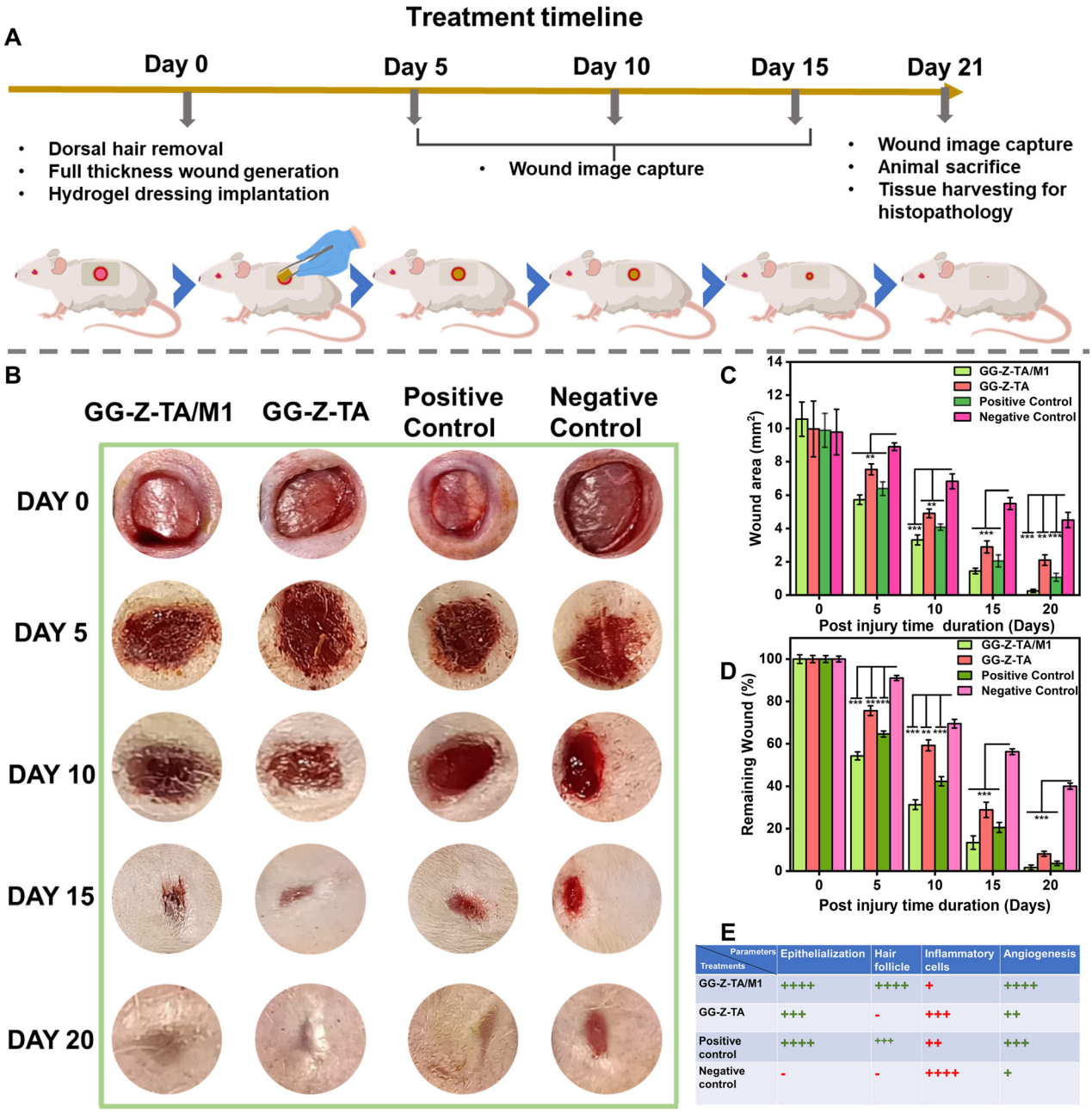

Parameters / Treatments	Epithelialization	Hair follicle	Inflammatory cells	Angiogenesis
GG-Z-TA/M1	++++	++++	+	++++
GG-Z-TA	+++	-	+++	++
Positive control	++++	+++	++	+++
Negative control	-	-	++++	+

Fig. 5 (A) Timeline of the *in vivo* wound-healing assay. (B) Macrographs of full-thickness wounds on rats at different time intervals. (C) Quantitative analysis of the wound area at certain time periods. (D) Quantitative analysis of remaining wound (%) at certain time periods. (E) Histological scoring of different parameters ((+) means present, (–) means absent). Here, columns and error bars signify the mean and standard deviation, whereas $*p < 0.05$, $**p < 0.005$, and $***p < 0.0005$ show the statistical difference.

remaining, whereas in the cases of GG-Z-TA, GG-Z-TA/M1, GG-Z-TA/M2, and GG-Z-TA/M3-treated groups, 71.79%, 32%, 24.5%, and 7.09% of the *E. coli*-formed biofilm was remaining. Similarly, for the GG-Z-TA, GG-Z-TA/M1, GG-Z-TA/M2, and GG-Z-TA/M3-treated groups, 83%, 51%, 45.25%, and 30.69% of the *S. aureus*-formed biofilm was remaining. It can be observed that, with an increase in the concentration of Cu-MOFs, the biofilm-inhibiting capacity of the hydrogels has been enhanced considerably. This observation correlates with the *in vitro* antibacterial evaluation, thus confirming the biofilm-inhibition efficacy of the hydrogels. In Fig. 4H, macrographic images of the crystal violet stain of the different treatment groups are presented. It can be observed that the color intensity of the bacterial culture gradually decreases as the concentration of Cu-MOFs increases, proving biofilm inhibition by the formulated hydrogels.

3.9. *In vivo* wound-healing efficacy

A rat full-thickness skin defect model was established to evaluate the wound-healing efficacy of the fabricated hydrogels as wound dressings, as shown in Fig. 5A. GG-Z-TA and GG-Z-TA/M1 hydrogels, having efficient biocompatibility, free radical scavenging activity, and bactericidal capacity, were defined as the blank and test groups, while treatment with Silverex was used as the positive control group. As shown in the macroscopic images of wounds at different time intervals (Fig. 5B), the wound area decreases over time for all the treatment groups, with GG-Z-TA/M1 showing remarkable healing of the wound that is even faster than that of the positive control. Quantitative analysis of the wound areas as depicted in Fig. 5C reveals that at each observation time interval in the case of the GG-Z-TA/M1 treatment group, the wound area has been reduced significantly compared to the other treatment groups. After day 21, the wound area was 0.25 mm^2 for the GG-Z-TA/M1 treatment group, whereas the wound area for the GG-Z-TA, positive control, and negative control groups was 2.1 mm^2, 1.05 mm^2, and 4.51 mm^2, respectively. To determine the wound healing rate, the remaining wound (%) was determined. As shown in Fig. 5D, for the GG-Z-TA/M1 treatment group, only 1.69% of the wound remains, in contrast to the other treatment groups, where the GG-Z-TA, positive control, and negative control treatment groups revealed that 6.1%, 3.62%, and 40% of the actual wound remains. Rats were sacrificed on day 21 and skin tissues were stained with hematoxylin and eosin (H&E) to estimate the advancement of wound healing.

In Fig. 6A, microscopic images of the H&E-stained skin tissue sections are presented. The images show that GG-Z-TA/M1 has promoted healing of the wound through extensive epidermis formation by regeneration of epithelial layers, formation of new blood vessels and creation of hair follicles. On the other hand, the GG-Z-TA and positive control treatment groups healed the wound to some extent through moderate epithelialization and neovascularization. However, in the case of untreated wounds, extensive inflammatory cell infiltration, absence of neovascularization, and negligible epithelialization led to unhealed wounds even after 21 days, presented as histological scoring in Fig. 5E. Also, the epidermal thickness of the H&E-stained skin tissue of the different treatment groups was determined through ImageJ software. Fig. 6B shows that the epidermal thickness of the control (–ve), control (+ve), GG-Z-TA and GG-Z-TA/M1-treated groups were 8.49 μm, 20.24 μm, 25.38 μm, and 27.45 μm, respectively. It also reveals that the GG-Z-TA/M1 formulation accelerated the wound-healing process through extensive re-epithelialization that finally led to the formation of a thicker epidermis compared to that in other treatment groups.

Overall, the fabricated Cu-MOF-loaded polymeric nanocomposite hydrogels accelerated wound healing compared to other treatments. The efficient wound healing capacity of the nano-composite polymeric hydrogels is mainly due to the bioactive role of TA and Cu-MOFs. The synergistic activity of TA and Cu-MOFs actually boosted the capacity of the fabricated hydrogels to expedite the wound-healing process through prevention of bacterial infection, scavenging excess free radicals, and stimulating angiogenesis and growth factor expression, together with collagen deposition.

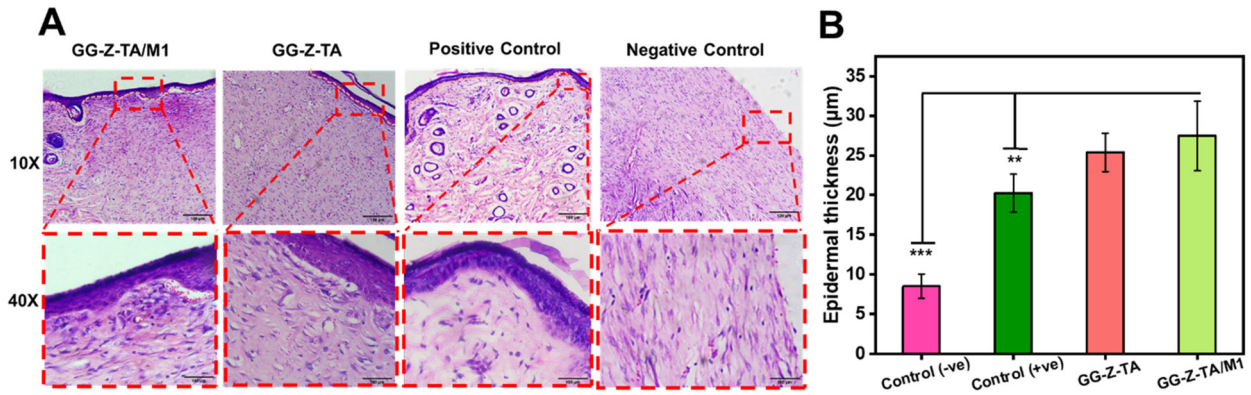

Fig. 6 (A) Histopathological analysis (H&E staining) of collected skin from wounds at day 21. (B) Epidermal thickness of the H&E-stained collected skin-tissue samples from different treatment groups. Here, columns and error bars signify the mean and standard deviation, whereas *$p < 0.05$, **$p < 0.005$, and ***$p < 0.0005$ show the statistical difference.

3. Conclusion

We developed multifunctional Cu-MOF, TA-loaded, physically crosslinked hydrogels composed of GG/Z. Cu-BTC MOFs were synthesized using a hydrothermal method through coordination between BTC and Cu ions. Cu-MOFs and TA were loaded physically into GG/Z-based polymeric hydrogels, which were further crosslinked with $CaCl_2$. Fabricated nano-composite polymeric hydrogels exhibited superior swelling capacity as a result of their interconnected microporous structure. Fabricated nano-composite polymeric hydrogels were biodegradable, hemocompatible, biocompatible against L929 fibroblast cells and had excellent free-radical scavenging properties. Incorporating Cu-MOFs into GG-Z-TA composite hydrogels enhanced the antibacterial activity of the polymeric hydrogels against both *E. coli* and *S. aureus*. Both TA and Cu ions were sustainably released from the hydrogel matrix for more than 4 days. Finally, in a rat full-thickness wound model, GG-Z-TA/M1 exhibited prominent wound-healing capability, and healed wounds to almost 100% as a result of the synergistic antibacterial activity, free-radical scavenging activity, and angiogenic activity of Cu ions and TA. The GG-Z-TA/M1 nanocomposite hydrogels may be suitable candidates as hydrogel wound dressings to treat chronic full-thickness wounds.

Author contributions

Aniruddha Dan: Conceptualization, Visualization, Investigation, Methodology, Writing-original draft, and editing, Software. **Ankita Panigrahi**: Investigation, Methodology, Writing-original draft, and editing. **Hemant Singh**: Conceptualization, Visualization, Methodology, Writing-original draft, **Manisha Meena:** Methodology, Original draft writing, and editing. **Varsha Murali:** Methodology, *In-vivo* study. **Prateek Goyel:** Preparation of Cu-MOFs, Methodology, editing. **Laxmanan Karthikeyan:** Original draft writing, Review & editing. **Superb K. Misra:** Resources, Review & editing. **Nibu Varghese:** Resources, *In-vivo* study, Review & editing. **Sharlene Sara Babu:** Resources, *In-vivo* study, Review & editing. **Yogesh B. Dalvi:** Resources, Investigation, *In-vivo* study, Review & editing. **Mukesh Dhanka:** Conceptualization, Supervision, Visualization, Investigation, Resources, Validation, original draft Review & editing. All authors have given their approval to the final version of the manuscript.

Data availability

All the data related to the study have been provided in the manuscript and its ESI.†

Conflicts of interest

The authors declare that they have no known competing financial interests or personal relationships that could have appeared to influence the work reported in this paper.

Acknowledgements

The authors acknowledge the Indian Institute of Technology Gandhinagar-Central Instrumentation Facility, with grants numbered IP/ITGN/BE/MD/2223/10 and IP/IITGN/BE/MD/2223/13. The authors would like to acknowledge the Pushpagiri Institute of Medical Sciences and Research Centre for assisting in the *in vivo* wound-healing studies on rat models. The authors wish to recognize Dr. Syed and Zenab Darban of Pandit Deendayal Energy University, Gandhinagar, Gujarat, for its instrumental facility.

References

1 A. H. Bacelar, J. Silva-Correia, J. M. Oliveira and R. L. Reis, *J. Mater. Chem. B*, 2016, **4**, 6164–6174.
2 B. Hu, M. Gao, K. O. Boakye-Yiadom, W. Ho, W. Yu, X. Xu and X. Q. Zhang, *Bioact. Mater.*, 2021, **6**, 4592–4606.
3 S. Chen, J. Lu, T. You and D. Sun, *Coord. Chem. Rev.*, 2021, **439**, 213929.
4 J. Andrade del Olmo, L. Pérez-Álvarez, V. Sáez-Martínez, S. Benito-Cid, L. Ruiz-Rubio, R. Pérez-González, J. L. Vilas-Vilela and J. M. Alonso, *Int. J. Biol. Macromol.*, 2022, **203**, 679–694.
5 L. P. Da Silva, R. L. Reis, V. M. Correlo and A. P. Marques. DOI: **10.1146/annurev-bioeng-060418**.
6 A. J. Littman, C. J. Knott, E. J. Boyko and S. E. Hawes, *Diabetes Care*, 2020, **43**, 956–963.
7 F. Xing, H. Ma, P. Yu, Y. Zhou, R. Luo, Z. Xiang, P. M. Rommens, X. Duan and U. Ritz, *Multifunctional metal–organic frameworks for wound healing and skin regeneration*, Elsevier Ltd, 2023, preprint, DOI: **10.1016/j.matdes.2023.112252**.
8 Q. Zhang, Y. Zhang, H. Chen, L. N. Sun, B. Zhang, D. S. Yue, C. L. Wang and Z. F. Zhang, *Sci. Rep.*, 2024, **14**, 1–13.
9 E. Caló and V. V. Khutoryanskiy, *Biomedical applications of hydrogels: A review of patents and commercial products*, 2015, Elsevier Ltd, DOI: **10.1016/j.eurpolymj.2014.11.024**.
10 S. Bhubhanil, C. Talodthaisong, M. Khongkow, K. Namdee, P. Wongchitrat, W. Yingmema, J. A. Hutchison, S. Lapmanee and S. Kulchat, *Sci. Rep.*, 2021, **11**, 1–14.
11 L. Gao, Y. Zhou, J. Peng, C. Xu, Q. Xu, M. Xing and J. Chang, *NPG Asia Mater.*, 2019, **11**, 1–11.
12 X. Zhang, Y. Li, D. He, Z. Ma, K. Liu, K. Xue and H. Li, *Chem. Eng. J.*, 2021, **425**, 130677.
13 Y. Jiang, C. Zhang, J. Yuan, Y. Wu, F. Li, G. I. N. Waterhouse, D. Li and Q. Huang, *Food Chem.*, 2021, **349**, 129112.
14 M. Dhanka, C. Shetty and R. Srivastava, *Int. J. Biol. Macromol.*, 2018, **110**, 346–356.
15 A. H. Bacelar, J. Silva-Correia, J. M. Oliveira and R. L. Reis, *J. Mater. Chem. B*, 2016, **4**, 6164–6174.
16 Y. Tang, J. Sun, H. Fan and X. Zhang, *Carbohydr. Polym.*, 2012, **88**, 46–53.

17 M. Jelkmann, C. Leichner, S. Zaichik, F. Laffleur and A. Bernkop-Schnürch, *Int. J. Biol. Macromol.*, 2020, **158**, 1037–1046.
18 N. A. Ismail, K. A. M. Amin, F. A. A. Majid and M. H. Razali, *Mater. Sci. Eng., C*, 2019, **103**, 109770.
19 J. Liu, R. Lai, X. Wang, H. Wang and Y. Liu, *Starch – Stärke*, 2020, **72**, 1900204.
20 Y. Wei, J. Yao, Z. Shao and X. Chen, *ACS Sustainable Chem. Eng.*, 2020, **8**, 7668–7679.
21 J. A. Tavares-Negrete, A. E. Aceves-Colin, D. C. Rivera-Flores, G. G. Díaz-Armas, A.-S. Mertgen, P. A. Trinidad-Calderón, J. M. Olmos-Cordero, E. G. Gómez-López, E. Pérez-Carrillo, Z. J. Escobedo-Avellaneda, A. Tamayol, M. M. Alvarez and G. Trujillo-De Santiago, Biofabrication using maize protein: 3D printing using zein formulations, *bioRxiv*, 2020, preprint, DOI: **10.1101/2020.07.29.227744**.
22 Y. Gong, C. Wang, R. C. Lai, K. Su, F. Zhang and D. A. Wang, *J. Mater. Chem.*, 2009, **19**, 1968–1977.
23 X. Zhang, Y. Pan, S. Li, L. Xing, S. Du, G. Yuan, J. Li, T. Zhou, D. Xiong, H. Tan, Z. Ling, Y. Chen, X. Hu and X. Niu, *Int. J. Biol. Macromol.*, 2020, **164**, 2204–2214.
24 C. Gering, J. Párraga, H. Vuorenpää, L. Botero, S. Miettinen and M. Kellomäki, *Biomater. Adv.*, 2022, **143**, 213185.
25 M. H. Al-Musawi, M. Rashidi, V. Mohammadzadeh, S. Albukhaty, E. Mahmoudi and M. Ghorbani, *J. Polym. Environ.*, 2023, **31**, 4738–4751.
26 S. Chen, C. Sun, Y. Wang, Y. Han, L. Dai, A. Abliz and Y. Gao, *J. Agric. Food Chem.*, 2018, **66**, 7441–7450.
27 U. Hayat, A. Raza and J. Y. Wang, *Polym. Degrad. Stab.*, 2020, **181**, 109303.
28 M. Allasia, A. S. Sonzogni, V. A. Vaillard, S. E. Vaillard, L. M. Gugliotta and R. J. Minari, *Polymer*, 2021, **235**, 124278.
29 A. Monfared, A. Ghaee and S. Ebrahimi-Barough, *IET Nanobiotechnol.*, 2019, **13**, 571–577.
30 M. Ghorbani, P. Nezhad-Mokhtari and S. Ramazani, *Int. J. Biol. Macromol.*, 2020, **153**, 921–930.
31 J. Gonçalves, N. Torres, S. Silva, F. Gonçalves, J. Noro, A. Cavaco-Paulo, A. Ribeiro and C. Silva, *React. Funct. Polym.*, 2020, **154**, 104664.
32 S. Ullah, M. Hashmi, J. Shi and I. S. Kim, *Polymers*, 2023, **15**(11), 2538.
33 C. Chen, X. Yang, S. Li, C. Zhang, Y. Ma, Y. Ma, P. Gao, S. Gao and X. Huang, *Green Chem.*, 2021, **23**, 1794–1804.
34 H. Fan, J. Wang, Q. Zhang and Z. Jin, *ACS Omega*, 2017, **2**, 6668–6676.
35 H. Jafari, P. Ghaffari-Bohlouli, S. V. Niknezhad, A. Abedi, Z. Izadifar, R. Mohammadinejad, R. S. Varma and A. Shavandi, Tannic acid: a versatile polyphenol for design of biomedical hydrogels, *J. Mater. Chem. B*, 2022, **10**(31), 5873–5912.
36 X. He, X. Liu, J. Yang, H. Du, N. Chai, Z. Sha, M. Geng, X. Zhou and C. He, *Carbohydr. Polym.*, 2020, **247**, 116689.
37 Y. Wu, W. Xu, J. Li, Z. Zhong, L. Huang, S. Li and H. Tan, *Eur. Polym. J.*, 2024, **202**, 112592.
38 H. Fan, J. Wang and Z. Jin, *Macromolecules*, 2018, **51**, 1696–1705.
39 C. Chen, H. Yang, X. Yang and Q. Ma, Tannic acid: a cross-linker leading to versatile functional polymeric networks: a review, *RSC Adv.*, 2022, **12**(13), 7689–7711.
40 J. Qu, X. Zhao, Y. Liang, T. Zhang, P. X. Ma and B. Guo, *Biomaterials*, 2018, **183**, 185–199.
41 H. Jafari, P. Ghaffari-bohlouli, D. Podstawczyk, L. Nie and A. Shavandi, *Carbohydr. Polym.*, 2022, **295**, 119844.
42 B. Ari, M. Sahiner, S. Demirci and N. Sahiner, *Polymers*, 2022, **14**(1), 70.
43 X. Feng, X. Hou, C. Cui, S. Sun, S. Sadik, S. Wu and F. Zhou, *Eng. Regener.*, 2021, **2**, 57–62.
44 G. Xu, N. Xu, T. Ren, C. Chen, J. Li, L. Ding, Y. Chen, G. Chen, Z. Li and Y. Yu, *Int. J. Biol. Macromol.*, 2022, **208**, 760–771.
45 J. E. Cun, X. Fan, Q. Pan, W. Gao, K. Luo, B. He and Y. Pu. Copper-based metal–organic frameworks for biomedical applications, *Advances in Colloid and Interface Science*, Elsevier B.V., 2022, vol. 305.
46 H. D. Lawson, S. P. Walton and C. Chan, *ACS Appl. Mater. Interfaces*, 2021, **13**, 7004–7020.
47 A. Wang, M. Walden, R. Ettlinger, F. Kiessling, J. J. Gassensmith, T. Lammers, S. Wuttke and Q. Peña, *Biomedical Metal–Organic Framework Materials:Perspectives and Challenges*, John Wiley and Sons Inc., 2023, DOI: **10.1002/adfm.202308589**.
48 M. Shen, F. Forghani, X. Kong, D. Liu, X. Ye, S. Chen and T. Ding, *Compr. Rev. Food Sci. Food Saf.*, 2020, **19**, 1397–1419.
49 A. Allahbakhsh, Z. Jarrahi, G. Farzi and A. Shavandi, *Mater. Chem. Phys.*, 2022, **277**, 125502.
50 C. Guo, F. Cheng, G. Liang, S. Zhang, Q. Jia, L. He, S. Duan, Y. Fu, Z. Zhang and M. Du, *Chem. Eng. J.*, 2022, **435**, 134915.
51 G. Wyszogrodzka, B. Marszałek, B. Gil and P. Dorozyński, *Drug Discov. Today*, 2016, **21**(6), 1009–1018.
52 R. Kaur, A. Kaur, R. Kaur, S. Singh, M. S. Bhatti, A. Umar, S. Baskoutas and S. K. Kansal, *Adv. Powder Technol.*, 2021, **32**, 1350–1361.
53 N. Philips, H. Hwang, S. Chauhan, D. Leonardi and S. Gonzalez, *Connect. Tissue Res.*, 2010, **51**, 224–229.
54 D. Bar-Or, G. W. Thomas, R. L. Yukl, L. T. Rael, R. P. Shimonkevitz, C. G. Curtis and J. V. Winkler, *Shock*, 2003, **20**, 154–158.
55 C. Gérard, L.-J. Bordeleau, J. Barralet and C. J. Doillon, *Biomaterials*, 2010, **31**, 824–831.
56 H. Singh, A. Dan, B. Prasanna Kumari, H. Dave, N. Parsaila, A. Navale, Z. Darban, I. Yadav, P. Goyal, S. K. Misra, S. Shahabuddin, S. Hassan and M. Dhanka, *Biomater. Adv.*, 2024, **164**, 213983.
57 P. Goyal, D. Menon, P. Jain, P. Prakash and S. K. Misra, *Sep. Purif. Technol.*, 2023, **318**, 123941.
58 S. Singh, D. Dutt, P. Kaur, H. Singh and N. C. Mishra, *J. Biomater. Sci., Polym. Ed.*, 2020, **31**, 1091–1106.
59 H. Singh, S. D. Purohit, R. Bhaskar, I. Yadav, S. Bhushan, M. K. Gupta and N. C. Mishra, *J. Biomed. Mater. Res., Part B*, 2022, **110**, 210–219.

60 H. Singh, S. Hassan, S. U. Nabi, N. C. Mishra, M. Dhanka, S. D. Purohit, N. A. Ganai, R. Bhaskar, S. S. Han, A. U. H. Qurashi and S. M. Bashir, *Int. J. Biol. Macromol.*, 2024, **255**, 127810.
61 H. Singh, S. D. Purohit, R. Bhaskar, I. Yadav, S. Bhushan, M. K. Gupta and N. C. Mishra, *J. Biomed. Mater. Res., Part B*, 2022, **110**, 210–219.
62 H. Singh, I. Yadav, W. M. Sheikh, A. Dan, Z. Darban, S. A. Shah, N. C. Mishra, S. Shahabuddin, S. Hassan, S. M. Bashir and M. Dhanka, *Int. J. Biol. Macromol.*, 2023, **251**, 126349.
63 Z. Neisi, Z. Ansari-Asl and A. S. Dezfuli, *J. Inorg. Organomet. Polym. Mater.*, 2019, **29**, 1838–1847.
64 M. S. Hosseini, S. Zeinali and M. H. Sheikhi, *Sens. Actuators, B*, 2016, **230**, 9–16.
65 R. Nivetha, A. Sajeev, A. M. Paul, K. Gothandapani, S. Gnanasekar, G. Jacob, R. Sellappan, V. Raghavan, N. K. Chandar, S. Pitchaimuthu, S. K. Jeong and A. N. Grace, *Mater. Res. Express*, 2020, **7**, 114001.
66 A. M. P. Peedikakkal and I. H. Aljundi, *ACS Omega*, 2020, **5**, 28493–28499.
67 Y. Liu, P. Ghimire and M. Jaroniec, *J. Colloid Interface Sci.*, 2019, **535**, 122–132.
68 B. Venu, V. Shirisha, B. Vishali, G. Naresh, R. Kishore, I. Sreedhar and A. Venugopal, *New J. Chem.*, 2020, **44**, 5972–5979.
69 C. Lin, X. Guo, F. Mo and D. Sun, *Int. J. Mol. Sci.*, 2023, **24**, 3173.
70 A. C. de Oliveira, R. M. Sabino, P. R. Souza, E. C. Muniz, K. C. Popat, M. J. Kipper, R. S. Zola and A. F. Martins, *Mater. Sci. Eng., C*, 2020, **106**, 110258.
71 N. Mamidi and R. M. Delgadillo, *ACS Appl. Mater. Interfaces*, 2024, **16**, 37468–37485.
72 C. Chen, X. W. Geng, Y. H. Pan, Y. N. Ma, Y. X. Ma, S. Z. Gao and X. J. Huang, *RSC Adv.*, 2020, **10**, 1724–1732.
73 J. Xiao, Y. Liang, T. Sun, M. Liu and X. He, *Sci. Rep.*, 2024, **14**, 1–16.
74 A. P. Serro, A. I. Fernandes, D. Silva, M. Ribeiro, M. Simões, C. Vitorino and F. Mascarenhas-Melo, *Gels*, 2024, **10**, 188.
75 M. H. Norahan, S. C. Pedroza-González, M. G. Sánchez-Salazar, M. M. Álvarez and G. Trujillo de Santiago, *Bioact. Mater.*, 2023, **24**, 197–235.
76 G. Eke, N. Mangir, N. Hasirci, S. MacNeil and V. Hasirci, *Biomaterials*, 2017, **129**, 188–198.
77 S. Anjum, A. Arora, M. S. Alam and B. Gupta, *Int. J. Pharm.*, 2016, **508**, 92–101.
78 X. Zhao, H. Wu, B. Guo, R. Dong, Y. Qiu and P. X. Ma, *Biomaterials*, 2017, **122**, 34–47.
79 D. Chouhan, T. u. Lohe, P. K. Samudrala and B. B. Mandal, *Adv. Healthcare Mater.*, 2018, **7**, 1801092.
80 C. Lazurko, Z. Khatoon, K. Goel, V. Sedlakova, C. Eren Cimenci, M. Ahumada, L. Zhang, T.-F. Mah, W. Franco, E. J. Suuronen and E. I. Alarcon, *ACS Biomater. Sci. Eng.*, 2020, **6**, 1124–1134.
81 N. Rashid, S. H. Khalid, I. U. Khan, Z. Chauhdary, H. Mahmood, A. Saleem, M. Umair and S. Asghar, *ACS Omega*, 2023, **8**, 7575–7586.
82 J. Ye, C. Shi, J. Lan, Q. Chen, Q. Si, P. Xu, X. Zhang and C. Zheng, *Sci. Rep.*, 2024, **14**, 1–14.
83 L. Yan, A. Gopal, S. Kashif, P. Hazelton, M. Lan, W. Zhang and X. Chen, *Chem. Eng. J.*, 2022, **435**(Part 2), 134975.
84 C. Pettinari, R. Pettinari, C. Di Nicola, A. Tombesi, S. Scuri and F. Marchetti, *Coord. Chem. Rev.*, 2021, **446**, 214121.
85 S. Elmehrath, K. Ahsan, N. Munawar, A. Alzamly, H. L. Nguyen and Y. Greish, *RSC Adv.*, 2024, **14**, 15821–15831.